

**A Comprehensive Solution for Whole-Brain multi-pool CEST Imaging at 3T based  
on single-shot True FISP readout: Towards Homogeneous, Multi-Parameter  
and High Repeatability**

Yupeng Wu <sup>a</sup>, Siyuan Fang <sup>a</sup>, Siyuan Wang <sup>b</sup>, Caixia Fu <sup>c</sup>, Jianqi Li <sup>a\*</sup>

<sup>a</sup> Shanghai Key Laboratory of Magnetic Resonance, School of Physics and Electronic Science,  
East China Normal University, Shanghai, China

<sup>b</sup> Zhejiang A&F University, Hangzhou, China

<sup>c</sup> MR Collaboration, Siemens (Shenzhen) Magnetic Resonance, Shenzhen, China

**\*Corresponding authors:**

Jianqi Li, Ph.D, Shanghai Key Laboratory of Magnetic Resonance, School of Physics and  
Electronic Science, East China Normal University, 3663 North Zhongshan Road, Shanghai,  
200062, China; Email: [jqli@phy.ecnu.edu.cn](mailto:jqli@phy.ecnu.edu.cn).

**Word count:** 2934

## Abstract

**Purpose:** To develop and validate a comprehensive, rapid, and reproducible solution for whole-brain, multi-pool Chemical Exchange Saturation Transfer (CEST) imaging at 3T, overcoming key barriers to clinical translation such as long acquisition times and inaccuracies from field inhomogeneities.

**Methods:** This study integrated a single-shot 3D true fast imaging with steady-state precession (True FISP) readout sequence for efficient whole-brain CEST data acquisition. A streamlined workflow was developed to acquire  $B_0$ ,  $B_1$ , and  $T_1$  maps for correction. To overcome the time-consuming nature of traditional  $B_1$  correction, we implemented a machine learning-based method, training a two-layer feed-forward neural network to perform rapid  $B_1$  correction using data from a single  $B_1$  power acquisition. Data were analyzed using a four-pool Lorentzian model to derive quantitative metrics, including magnetization transfer ratio based on Lorentzian difference (MTR<sub>LD</sub>) and the confounder-corrected Apparent Exchange-dependent Relaxation (AREX). The method's accuracy was validated in phantoms and its test-retest reproducibility was assessed in healthy volunteers across 96 brain regions.

**Results:** The True FISP sequence acquired high-quality, whole-brain images free of major artifacts. The neural network accurately replicated the gold-standard three-point  $B_1$  correction, achieving excellent intraclass correlation (ICC > 0.97) in human subjects. The AREX metric successfully corrected for  $T_1$  and MT confounders, reducing the coefficient of variation (CV) from 35.4% to 9.2% in phantoms. The complete pipeline, including Z-spectrum and correction maps, took approximately 9 minutes. The method demonstrated high region-level reproducibility, with the average CV for APT\_AREX under 10% for most brain regions across test-retest scans.

**Conclusion:** This study presents a validated, end-to-end solution for whole-brain, multi-pool CEST imaging. By combining an efficient sequence with a rapid, AI-driven correction pipeline and robust quantitative analysis, our method delivers high-fidelity, reproducible, and quantitative multi-parameter maps of brain metabolism in a clinically acceptable timeframe.

**Keywords:** CEST, whole-brain, multi-pool, true fast imaging with steady-state precession (True FISP), balanced steady state free precession (bSSFP)

## 1 INTRODUCTION

Chemical Exchange Saturation Transfer (CEST)<sup>1-4</sup> is a powerful molecular imaging technique that enables the detection of molecules and physiological parameters, such as proteins and pH levels, non-invasively. This capability has made it highly valuable in clinical research, particularly in the fields of oncology and neurology for applications like cancer<sup>5-8</sup> and stroke studies<sup>2,9,10</sup>. There is a growing body of evidence from both preclinical and clinical studies suggesting that CEST imaging holds significant promise for diagnosing neurodegenerative diseases by revealing their specific metabolic processes.<sup>11-14</sup> Specifically, multi-pool CEST<sup>5,8,15,16</sup>, which provides information from multiple molecular sources simultaneously, enhances diagnostic efficiency and improves the interpretability of imaging results.

For diseases that affect multiple brain regions and gray matter nuclei, such as neurodegenerative disorders, whole-brain CEST imaging is particularly advantageous as it facilitates comprehensive, region-of-interest-based analysis and improves the efficiency of clinical research. However, a significant bottleneck for the clinical translation of multi-pool CEST is the limited signal acquisition efficiency of current methods. Most clinical studies<sup>8,12,14,17</sup> are restricted to single-slice or partial brain acquisitions, which severely limits the technique's practical utility.

Furthermore, the accuracy of CEST imaging is often compromised by hardware-related magnetic field inhomogeneities, namely  $B_0$  (main magnetic field) and  $B_1$  (transmit radio-frequency field). While metrics like the apparent exchange-dependent relaxation (AREX)<sup>5,18</sup> have been proposed to correct for confounding factors such as water spillover effects, magnetization transfer (MT), and  $T_1$  relaxation, their implementation is challenging. Acquiring the necessary correction maps ( $B_0$ ,  $B_1$ , and  $T_1$  maps) with conventional sequences is prohibitively time-consuming. Moreover, traditional  $B_1$  correction methods necessitate repeated Z-spectrum acquisitions, further increasing the scan time and hindering clinical adoption.<sup>19</sup> Compounding these issues, the reproducibility of previously proposed whole-brain multi-pool CEST methods has not been validated at the brain-region level, creating uncertainty about their reliability for clinical use.

To address these limitations, our recent work<sup>20</sup> has shown that a single-shot 3D multi-pool

CEST sequence based on a true fast imaging with steady-state precession (True FISP) readout, also known as balanced steady-state free precession (bSSFP), offers a higher signal-to-noise ratio (SNR) compared to conventional spoiled GRE readouts within the same acquisition time, demonstrating significant potential for clinical translation. Building on this foundation, this study aims to further optimize the True FISP-based CEST sequence and develop a comprehensive solution for clinically applicable, whole-brain, multi-pool CEST imaging. To achieve this, we focused on the following objectives: (1) to optimize and validate a whole-brain multi-pool CEST sequence based on the True FISP readout; (2) to develop rapid acquisition sequences for  $B_0$ ,  $B_1$ , and  $T_1$  maps and to validate the effectiveness of  $B_1$  correction and the AREX metric in phantoms; (3) to integrate and validate a neural network model<sup>21</sup> for rapid  $B_1$  correction, a technique that has shown promise for reducing scan times, and to validate its performance in human subjects; and (4) to verify the region-level reproducibility of the derived CEST metrics in healthy subjects.

## 2 METHODS

### 2.1 MRI Acquisition

This study was approved by the local institutional review board, and all participants provided written informed consent. All experiments were performed on a 3T whole-body MRI system (MAGNETOM Prisma Fit; Siemens Healthcare, Erlangen, Germany) with a 64-channel Head/Neck coil.

#### 2.1.1 Whole-Brain CEST Protocol

The core of this study is a custom CEST sequence composed of a pre-saturation module and a single-shot 3D True FISP readout.

- **Saturation Module:** A series of 28 Gaussian-shaped RF pulses (100 ms duration each) were applied for pre-saturation. A crusher gradient was used in the 5-ms interval between pulses to eliminate residual transverse magnetization. The total saturation time ( $t_{\text{Sat}}$ ) was 3.0 seconds with an average  $B_1$  amplitude of 0.7  $\mu\text{T}$ , followed by a fat saturation module.
- **Readout Module:** A 3D True FISP sequence with centric spiral reordering and alternating-phase RF excitation was used for data acquisition. To minimize signal oscillations, a

preparatory half-flip-angle pulse was employed.

- **Imaging Parameters:** Key parameters were set as follows: TR/TE = 2/1 ms, flip angle = 25°, FOV = 220 × 220 × 200 mm<sup>3</sup>, matrix size = 88 × 88 × 80, and voxel size = 2.5 × 2.5 × 2.5 mm<sup>3</sup>. The short TR was chosen to prevent banding artifacts. GRAPPA acceleration (2 × 2) and elliptical sampling were used, resulting in a readout time (t<sub>RO</sub>) of 3.6 s. The total time per frequency offset was 6.6 s (t<sub>sat</sub> + t<sub>RO</sub>).
- **Z-Spectrum Sampling:** Data were collected at 55 frequency offsets, including reference scans at -300 ppm and a dense sampling around the water peak, for a total Z-spectrum scan time of approximately 6.0 minutes.

### 2.1.2 Correction Map and Anatomical Imaging

For subsequent corrections, maps of the main magnetic field offset ( $\Delta B_0$ ), relative transmit field ( $rB_1$ ), and  $T_1$  relaxation time were acquired sequentially using a dual-echo modified four-angle method<sup>22</sup>, with a scan time of 3.0 minutes. Detailed scanning parameters for this acquisition are provided in the Supporting Information (Table S1). Additionally, a high-resolution  $T_1$ -weighted MP-RAGE image was acquired from each volunteer for anatomical reference.

### 2.1.3 Experimental Cohorts

- **Phantom Studies:** Two phantoms were used. The first, containing six tubes of 8% polylysine and 1% agarose (pH=7.3), was used to validate the three-point  $B_1$  correction method<sup>19</sup>. The second, containing tubes with varying concentrations of agarose and gadolinium, was used to test the efficacy of the AREX metric in correcting for  $T_1$  and MT effects.
- **Human Studies:** Eight healthy volunteers participated. Four subjects were scanned at three saturation powers (0.5, 0.7, and 1.0  $\mu$ T) to provide data for training and validating the  $B_1$ -correction neural network. A separate cohort of four healthy subjects was scanned twice on alternate days to assess the method's test-retest reproducibility.

## 2.2 Data Processing and Analysis

A multi-step pipeline was implemented for data processing.

### 2.2.1 Image Pre-processing and Correction Map Generation

First, all raw CEST images were aligned to the unsaturated reference image ( $S_0$ ) using a rigid registration (SPM 12) to correct for subject motion. The images were then denoised slice-by-slice using a deep-learning model. Concurrently, the  $\Delta B_0$ ,  $rB_1$ , and  $T_1$  maps were calculated from the dedicated multi-echo, multi-angle acquisition.

### 2.2.2 Z-Spectrum Correction

The normalized Z-spectrum ( $Z(\Delta\omega) = S_{\text{sat}}(\Delta\omega)/S_0$ ) was corrected for magnetic field inhomogeneities.

- 1)  **$B_0$  Correction:** The Z-spectrum of each voxel was shifted along the frequency axis based on its corresponding  $\Delta B_0$  value after interpolation to a 1-Hz resolution.
- 2)  **$B_1$  Correction:** Two methods for  $B_1$  correction were employed.
  - The traditional three-point method was applied to all phantom data and the first human cohort (scanned at three  $B_1$  powers) to generate accurately corrected Z-spectra at a nominal  $B_1$  of 0.7  $\mu\text{T}$ .
  - For rapid correction, we adapted the machine learning approach for  $B_1$  correction inspired by Leonie Hunger et al<sup>21</sup>. Specifically, a two-layer feed-forward neural network with 15 neurons in the hidden layer was implemented and trained. This was accomplished using the Neural Network Fitting application within MATLAB (The MathWorks, Natick, MA). The network architecture consisted of a hidden layer with a hyperbolic tangent sigmoid activation function (tansig) and a linear output layer (purelin), a standard configuration for non-linear function approximation. The network was trained using the Levenberg-Marquardt backpropagation algorithm (trainlm). Using data from three subjects, the uncorrected Z-spectra from the nominal 0.7  $\mu\text{T}$  acquisition and  $rB_1$  maps were used as inputs, with the Z-spectra corrected by the three-point method serving as the target output.

### 2.2.3 Quantitative CEST Analysis

Corrected Z-spectra were analyzed voxel-wise using a four-pool Lorentzian model that included contributions from direct water saturation (0 ppm), magnetization transfer (MT, -1.0 ppm), nuclear Overhauser enhancement (NOE, -3.5 ppm), and amide proton transfer (APT, +3.5 ppm).

The model function is given by:

$$Z(\Delta\omega) = 1 - \sum_{i=1}^4 L_i(\Delta\omega), \text{ where } L_i(\Delta\omega) = A_i \frac{W_i^{2/4}}{W_i^{2/4} + (\Delta\omega - \Delta_i)^2}.$$

Here,  $A_i$ ,  $\Delta_i$ , and  $W_i$  are the amplitude, frequency offset, and full width at half maximum of the  $i$ -th Lorentzian pool.

From the fitted model, two quantitative metrics were derived:

- 1) **MTR<sub>LD</sub>:** The magnetization transfer ratio based on Lorentzian difference, calculated as  

$$\text{MTR}_{\text{LD}}(\Delta\omega) = Z_{\text{ref}}(\Delta\omega) - Z_{\text{lab}}(\Delta\omega).$$
- 2) **AREX:** An apparent exchange-dependent relaxation metric corrected for spillover, MT, and  $T_1$  effects, calculated as  

$$\text{AREX}(\Delta\omega) = (Z_{\text{lab}}(\Delta\omega)^{-1} - Z_{\text{ref}}(\Delta\omega)^{-1})/T_1,$$
where  $T_1$  is the tissue longitudinal relaxation time measured from the correction scan.

#### 2.2.4 Regional Analysis

For region-of-interest (ROI) analysis, the subject's unsaturated reference image was registered to their high-resolution  $T_1$ -weighted image. The  $T_1$ -weighted image was then segmented into 96 distinct brain regions and nuclei using FreeSurfer (<https://surfer.nmr.mgh.harvard.edu/>). These ROIs were subsequently mapped onto the quantitative CEST images to extract the average value of each metric within every defined brain region.

### 3 RESULTS

#### 3.1 High-Fidelity Whole-Brain Image Acquisition without Major Artifacts

The custom single-shot 3D True FISP sequence successfully acquired high-quality, whole-

brain unsaturated reference images ( $M_0$ ). As shown in a representative slice in Figure 1, the  $M_0$  images are sharp and notably free of the banding artifacts that can affect bSSFP acquisitions. Furthermore, in regions prone to magnetic susceptibility artifacts, such as near the nasal cavity, the  $M_0$  images demonstrated a level of artifact suppression comparable to that of the anatomical MP-RAGE images, with minimal geometric distortion. The main magnetic field shift ( $\Delta B_0$ ) was less than 2 ppm across the vast majority of brain tissue. For human studies, the saturation protocol using a  $B_1$  amplitude of 0.7  $\mu\text{T}$  resulted in an average Specific Absorption Rate (SAR) of  $52\% \pm 6.8\%$  of the IEC normal operating mode limit, which is well within acceptable safety limits.

### **3.2 Validation and Rapid Implementation of $B_1$ Correction**

#### **3.2.1 Validation of the Three-Point $B_1$ Correction Method in Phantoms**

The efficacy of the traditional three-point  $B_1$  correction method was first validated in a phantom study (Figure 2). The phantom's  $rB_1$  map showed lower values at the periphery compared to the center. Before correction, the  $MT\_MTR_{LD}$  map exhibited a clear spatial distribution corresponding to the  $rB_1$  map. After applying the three-point correction, this dependency was eliminated, and the  $MT\_MTR_{LD}$  values across the six test tubes became consistent. This improvement is quantified in Table 1, where the coefficient of variation (CV) for  $MT\_MTR_{LD}$  decreased significantly from 22.49% to 4.61% post-correction. In contrast, the CV for  $APT\_MTR_{LD}$  remained low (around 5%) both before and after correction.

#### **3.2.2 Training and Performance of a Neural Network for Rapid $B_1$ Correction**

The rapid  $B_1$  correction strategy, which utilizes a two-layer feed-forward neural network with 15 hidden neurons, was successfully implemented and trained using the study's data. The model was trained for 18 hours and demonstrated excellent performance, achieving a high correlation ( $R \approx 0.9997$ ) and low mean squared error ( $MSE \approx 1.7-1.8 \times 10^{-5}$ ) on the training, validation, and testing datasets (Table 2).

The performance of the neural network was validated in human subjects by comparing its output to the gold-standard three-point method (Figure 3). Without  $B_1$  correction,  $MTR_{LD}$  maps, particularly for the MT effect, showed a clear signal reduction in regions with low  $B_1$ , such as the frontal lobe, creating a spatial pattern similar to the  $rB_1$  map. The difference images between

the neural network-corrected and three-point-corrected  $\text{MTR}_{\text{LD}}$  maps showed only minimal residual values for APT, NOE, and MT effects, indicating a high degree of agreement.

This agreement was quantified via a regional analysis across 96 brain regions (Table 3). The intraclass correlation coefficient (ICC) between the neural network and the three-point method was excellent for all effects: APT\_MTR<sub>LD</sub> (0.975), NOE\_MTR<sub>LD</sub> (0.985), and MT\_MTR<sub>LD</sub> (0.997). In contrast, the ICC between the uncorrected data and the three-point method was substantially lower for the MT effect (0.830).

### 3.3 Efficacy of the AREX Metric for Confounder Correction

The ability of the AREX metric to correct for confounding  $T_1$  and MT effects was demonstrated in a custom phantom (Figure 4). In this phantom, tubes containing the same concentration of polylysine were prepared with varying amounts of gadolinium and agarose to alter their  $T_1$  and MT properties. As a result, the APT\_MTR<sub>LD</sub> metric showed significant signal differences among these tubes. However, the APT\_AREX metric successfully corrected for these confounders, yielding similar and consistent signal intensities across the tubes, thereby isolating the desired chemical exchange effect. Quantitatively, the use of AREX reduced the coefficient of variation across the five test tubes (A, B1, B2, C1, and C2) containing 8% polylysine from 35.4% (APT\_MTR<sub>LD</sub>) to a mere 9.2% (APT\_AREX).

### 3.4 Whole-Brain Multi-Parameter CEST Imaging and Regional Reproducibility

By integrating the True FISP sequence with the validated neural network  $B_1$  correction and quantitative analysis, we generated whole-brain, multi-parameter CEST maps (Figure 5). When comparing quantitative metrics, AREX maps exhibited enhanced gray-white matter contrast compared to their  $\text{MTR}_{\text{LD}}$  counterparts, an effect that was particularly evident in the NOE and MT images. The underlying four-pool Lorentzian model provided a high-quality fit to the experimental data, with the fitting residual for the Z-spectrum being less than 1.0% in a representative voxel (Figure 6).

Finally, the method's test-retest reproducibility was assessed in a cohort of four healthy subjects scanned on alternate days. The analysis demonstrated high reproducibility at the brain-region level. As shown in Figure 7, the average coefficient of variation for the APT\_AREX metric across 96 brain regions was less than 10% for the majority of regions, confirming the

robustness of the proposed imaging solution for reliable, region-of-interest-based analysis. The reproducibility analyses for the other quantitative metrics (NOE\_AREX, MT\_AREX, and all MTR<sub>LD</sub> metrics) are provided in the Supporting Information (Figures S1-S5)

## 4 DISCUSSIONS

In this study, we developed and validated a comprehensive solution for whole-brain, multi-pool CEST imaging at 3T that is rapid, accurate, and highly reproducible. Our approach successfully integrates a single-shot 3D True FISP readout sequence with a streamlined workflow for B<sub>0</sub>, B<sub>1</sub>, and T<sub>1</sub> correction, highlighted by the implementation of a neural network for rapid B<sub>1</sub> field inhomogeneity correction. By addressing several critical bottlenecks that have historically hindered the clinical translation of CEST, our work provides a practical pathway for its application in diseases affecting multiple brain regions, such as neurodegenerative disorders.

A cornerstone of our method is the use of a single-shot 3D True FISP readout, which we previously showed offers a superior SNR compared to conventional spoiled GRE acquisitions within the same timeframe. Here, we demonstrated that this sequence can acquire high-quality, whole-brain images free of the banding artifacts typically associated with bSSFP techniques, even in regions with high magnetic susceptibility. The total acquisition time for a 55-point Z-spectrum was approximately 6.0 minutes, and the necessary correction maps were acquired in just 3.0 minutes. This efficiency is a significant step towards overcoming the limited signal acquisition efficiency that has confined most clinical CEST studies to single-slice or partial brain coverage.

The accuracy of CEST imaging is critically dependent on correcting for magnetic field inhomogeneities, particularly B<sub>1</sub>, which can be prohibitively time-consuming with traditional methods. Our study tackled this challenge directly. First, we confirmed the efficacy of the established three-point B<sub>1</sub> correction method in phantoms, which effectively removed B<sub>1</sub>-dependent variations in MT\_MTR<sub>LD</sub>, reducing its coefficient of variation from 22.49% to 4.61%. This provided a reliable gold standard. Building on foundational work by Leonie Hunger et al<sup>21</sup>, we successfully implemented, trained, and validated a custom neural network for our specific True FISP CEST data. Our custom-trained two-layer feed-forward neural

network accurately replicates the results of the three-point method but without the need for additional scans at different power levels. The network demonstrated exceptional performance, with the corrected MTR<sub>LD</sub> values showing an excellent intraclass correlation (ICC > 0.97) with the gold standard across all CEST effects in human subjects. This integration effectively eliminates the prolonged scan times associated with multi-power acquisitions, making comprehensive B<sub>1</sub> correction feasible within a clinical workflow.

Beyond field corrections, the interpretability of CEST metrics is often confounded by factors like T<sub>1</sub> relaxation and MT effects. Our work validates the utility of the AREX metric to mitigate these confounders. In a phantom designed with varying T<sub>1</sub> and MT properties, the APT\_MTR<sub>LD</sub> metric showed significant variability (CV = 35.4%) that did not reflect the true chemical exchange. In contrast, the APT\_AREX metric successfully corrected for these effects, yielding consistent values across the tubes (CV = 9.2%) and isolating the desired exchange effect. In human subjects, AREX maps consistently showed enhanced gray-white matter contrast compared to MTR<sub>LD</sub> maps, suggesting improved biological specificity. This confirms that the combination of our acquisition strategy and the AREX calculation provides a more robust and unbiased measure of metabolic activity.

A final, crucial contribution of this work is the rigorous assessment of test-retest reproducibility, a validation that has been absent in previously proposed whole-brain CEST methods. Our results demonstrated high reproducibility at the brain-region level, with the average coefficient of variation for APT\_AREX across 96 distinct brain regions being less than 10% for the majority of regions in healthy subjects scanned on alternate days. This level of robustness is essential for clinical applications, particularly for longitudinal monitoring of disease progression or treatment response, and for cross-sectional studies comparing different patient groups.

This study has several limitations. First, the validation was conducted exclusively in healthy volunteers, so the method's clinical utility must be established in patient populations. Second, the neural network was trained on a single 3T MRI system, and its generalizability to other scanners requires further investigation and potential retraining. Additionally, while the total acquisition time of approximately 9 minutes is clinically acceptable, further acceleration could improve workflow efficiency. The analysis also relied on a simplified four-pool

Lorentzian model; more advanced modeling could enhance the specificity of the derived metrics. Finally, the choice of a 3-second saturation time represents a trade-off between achieving a saturation steady-state and maintaining a clinically feasible scan time. While this duration may not achieve a full steady state for all exchange regimes, which could slightly impair the absolute accuracy of AREX correction, it was deemed necessary for the overall rapid protocol. Future work could explore overcoming this limitation without extending the scan time by employing advanced reconstruction techniques like QUASS<sup>7</sup>.

## 5 CONCLUSIONS

In conclusion, this study presents a validated, end-to-end solution for whole-brain multi-pool CEST imaging. By combining an efficient True FISP sequence with a rapid, AI-driven correction pipeline and robust quantitative analysis, our method overcomes major barriers to clinical adoption. It delivers high-fidelity, reproducible, and quantitative multi-parameter maps of brain metabolism in a clinically acceptable timeframe, holding significant promise for advancing neuro-imaging research and diagnostics.

## ACKNOWLEDGMENTS

## DATA AVAILABILITY STATEMENT

The data that support the findings of this study are available from the corresponding author upon reasonable request.

## REFERENCES

1. Ward KM, Aletras AH, Balaban RS. A new class of contrast agents for MRI based on proton chemical exchange dependent saturation transfer (CEST). *J Magn Reson.* 2000;143:79–87.
2. Zhou JY, Payen JF, Wilson DA, Traystman RJ, van Zijl PCM. Using the amide proton signals of intracellular proteins and peptides to detect pH effects in MRI. *Nat Med.* 2003;9:1085–1090.
3. van Zijl PCM, Yadav NN. Chemical exchange saturation transfer (CEST): What is in a name and what isn't? *Magn Reson Med.* 2011;65:927–948.
4. van Zijl PCM, Lam WW, Xu JD, Knutsson L, Stanisz GJ. Magnetization transfer contrast and chemical exchange saturation transfer MRI. Features and analysis of the field-dependent saturation

spectrum. *Neuroimage*. 2018;168:222-241.

- 5. Zaiss M, Windschuh J, Paech D, et al. Relaxation-compensated CEST-MRI of the human brain at 7T: Unbiased insight into NOE and amide signal changes in human glioblastoma. *Neuroimage*. 2015;112:180-188.
- 6. Zhou JY, Zaiss M, Knutsson L, et al. Review and consensus recommendations on clinical APT-weighted imaging approaches at 3T: Application to brain tumors. *Magn Reson Med*. 2022;88:546-574.
- 7. Sun PZ. Quasi-steady-state (QUASS) reconstruction enhances normalization in apparent exchange-dependent relaxation (AREX) analysis: A reevaluation of correction in quantitative CEST MRI of rodent brain tumor models. *Magn Reson Med*. 2024;92:236-245.
- 8. Zhu HQ, Li YH, Ding YJ, et al. Multi-pool chemical exchange saturation transfer MRI in glioma grading, molecular subtyping and evaluating tumor proliferation. *J Neurooncol*. 2024;169:287-297.
- 9. Longo DL, Cutrin JC, Michelotti F, Irrera P, Aime S. Noninvasive evaluation of renal pH homeostasis after ischemia reperfusion injury by CEST-MRI. *NMR Biomed*. 2017;30.
- 10. Wang KX, Ju LC, Qiao GD, et al. Elucidating metabolite and pH variations in stroke through guanidino, amine and amide CEST MRI: A comparative multi-field study at 9.4T and 3T. *Neuroimage*. 2025;305.
- 11. Huang JP, Lai JHC, Tse KH, et al. Deep neural network based CEST and AREX processing: Application in imaging a model of Alzheimer's disease at 3 T. *Magn Reson Med*. 2022;87:1529-1545.
- 12. Zhu DY, Fu XN, Liu J, et al. Multiparametric chemical exchange saturation transfer MRI detects metabolic changes in mild cognitive impairment cases at 3.0 Tesla. *Neurochem Res*. 2025;50.
- 13. Mennecke A, Khakzar KM, German A, et al. 7 tricks for 7 T CEST: Improving the reproducibility of multipool evaluation provides insights into the effects of age and the early stages of parkinson's disease. *NMR Biomed*. 2023;36.
- 14. Tian YT, Li XY, Chen HB, et al. Altered nigral amide proton transfer imaging signal concordant with motor asymmetry in parkinson's disease: A multipool CEST MRI study. *NMR Biomed*. 2025;38.
- 15. Heo HY, Zhang Y, Jiang SS, Lee DH, Zhou JY. Quantitative assessment of amide proton transfer (APT) and nuclear Overhauser enhancement (NOE) imaging with extrapolated semisolid magnetization transfer reference (EMR) signals: II. Comparison of three EMR models and application to human brain glioma at 3 Tesla. *Magn Reson Med*. 2016;75:1630-1639.
- 16. Sun PZ. Demonstration of accurate multi-pool chemical exchange saturation transfer MRI quantification-quasi-steady-state reconstruction empowered quantitative CEST analysis. *J Magn Reson*. 2023;348.
- 17. Su CL, Xu SJ, Lin DL, et al. Multi-parametric z-spectral MRI may have a good performance for glioma stratification in clinical patients. *Eur Radiol*. 2022;32:101-111.
- 18. Zaiss M, Xu JZ, Goerke S, et al. Inverse Z-spectrum analysis for spillover-, MT-, and T1-corrected steady-state pulsed CEST-MRI - application to pH-weighted MRI of acute stroke. *NMR Biomed*. 2014;27:240-252.
- 19. Windschuh J, Zaiss M, Meissner JE, et al. Correction of B1-inhomogeneities for relaxation-compensated CEST imaging at 7T. *NMR Biomed*. 2015;28:529-537.
- 20. Wu. Y, Pang. Q, Wang. Z, et al. 3D single-shot CEST imaging at 3T based on True FISP readout. arXiv preprint. 2025;arXiv:2501.03548.

21. Hunger L, Rajput JR, Klein K, et al. Deepcest 7 T: Fast and homogeneous mapping of 7 T CEST MRI parameters and their uncertainty quantification. *Magn Reson Med.* 2023;89:1543-1556.
22. Bouhrara M, Rejimon AC, Cortina LE, Khattar N, Spencer RG. Four-angle method for practical ultra-high-resolution magnetic resonance mapping of brain longitudinal relaxation time and apparent proton density. *Magn Reson Imaging.* 2020;66:57-68.

Table 1. Comparison of Measurement Variability in Phantom MTR<sub>LD</sub> Metrics Before and After B<sub>1</sub> Correction.

Metric	CV (%) Before B <sub>1</sub> Correction	CV (%) After B <sub>1</sub> Correction
APT_MTR <sub>LD</sub>	4.44%	5.16%
MT_MTR <sub>LD</sub>	22.49%	4.61%

Table 2. Performance metrics of the neural network model for B<sub>1</sub> correction.

Dataset	Sample size	MSE	R
Training	215350	1.7540 x 10 <sup>-5</sup>	0.99975
Validation	46147	1.7475 x 10 <sup>-5</sup>	0.99975
Testing	46147	1.7932 x 10 <sup>-5</sup>	0.99974

**Note:** MSE: Mean Squared Error; R: Correlation Coefficient.

Table 3. Intraclass Correlation Coefficients (ICCs) for Regional MTR<sub>LD</sub> Metrics Across Different B<sub>1</sub> Correction Methods.

Comparison Method	APT_MTR <sub>LD</sub>	NOE_MTR <sub>LD</sub>	MT_MTR <sub>LD</sub>
Uncorrected vs. Three-Point Method	0.909 [0.821, 0.948]	0.997 [0.994, 0.999]	0.830 [0.723, 0.893]
Neural Network vs. Three-Point Method	0.975 [0.963, 0.983]	0.985 [0.977, 0.990]	0.997 [0.995, 0.998]

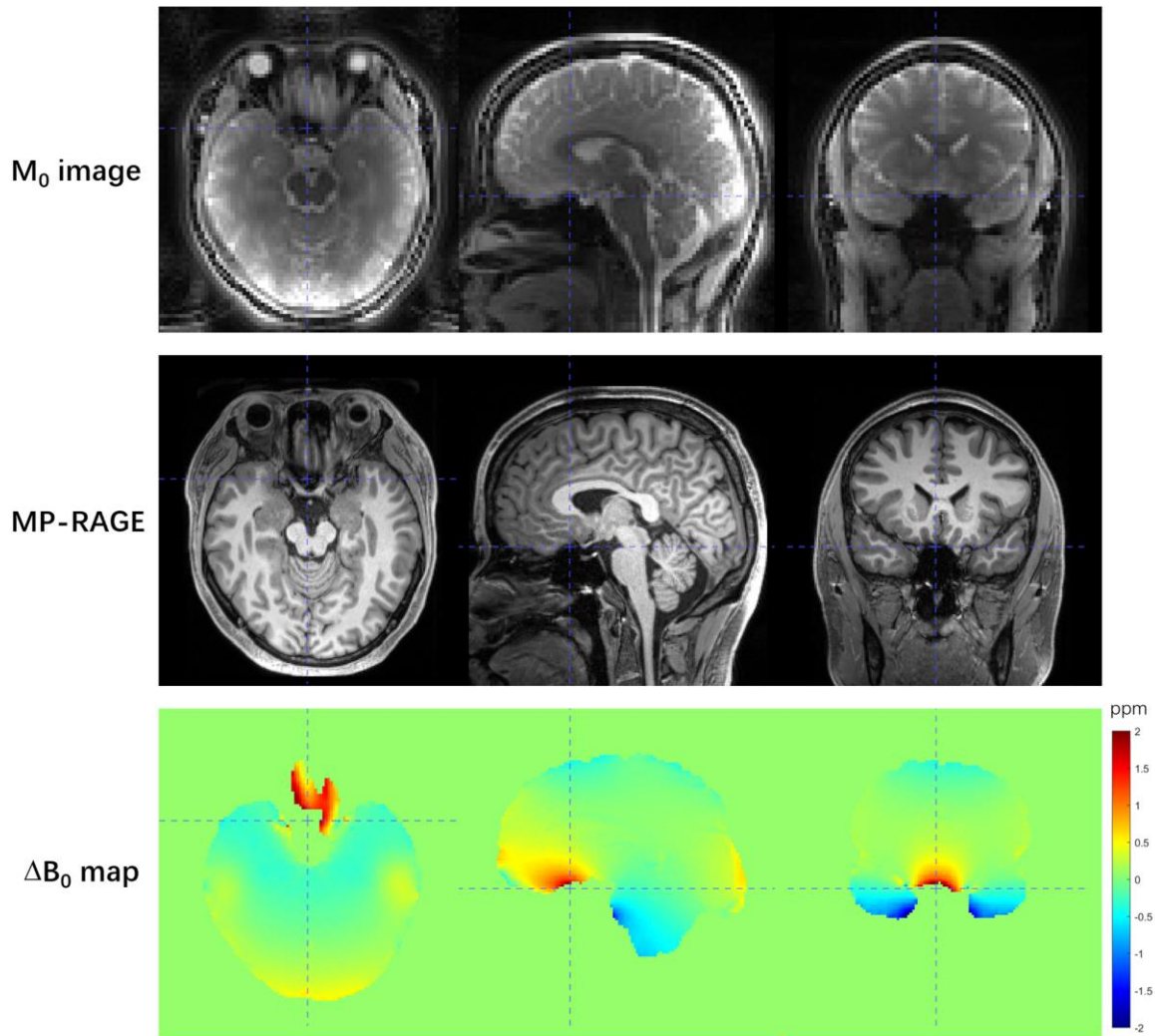


Figure 1. High-quality whole-brain image acquisition using the single-shot 3D True FISP sequence. Representative slices show the unsaturated reference image ( $M_0$ ), the corresponding anatomical  $T_1$ -weighted MP-RAGE image, and the main magnetic field offset ( $\Delta B_0$ ) map. The  $M_0$  image is notably free of banding artifacts and shows minimal susceptibility-induced distortion, with a level of artifact suppression in challenging regions that is comparable to the MP-RAGE reference.

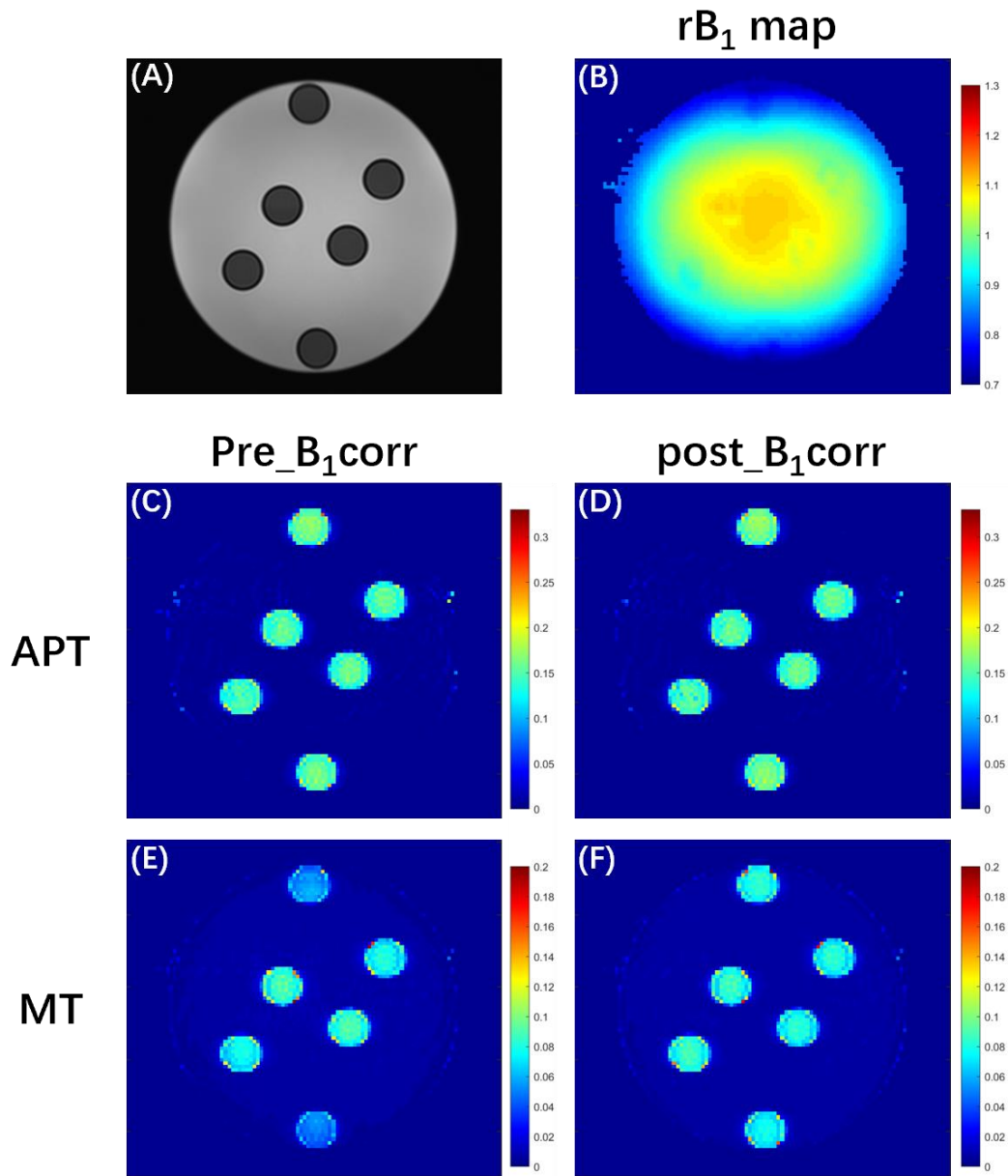


Figure 2. Validation of the three-point B<sub>1</sub> correction method in a custom phantom. (A) Schematic of the phantom, consisting of six tubes with 8% polylysine and 1% agarose (pH=7.3). (B) The measured relative transmit field (rB<sub>1</sub>) map, showing significant inhomogeneity. (C, D) Amide Proton Transfer (APT\_MTR<sub>LD</sub>) maps are shown before (C) and after (D) B<sub>1</sub> correction. (E, F) Magnetization Transfer (MT\_MTR<sub>LD</sub>) maps are shown before (E) and after (F) B<sub>1</sub> correction. The correction visibly homogenizes the MT\_MTR<sub>LD</sub> map, removing the spatial dependency on the rB<sub>1</sub> distribution seen in (E).

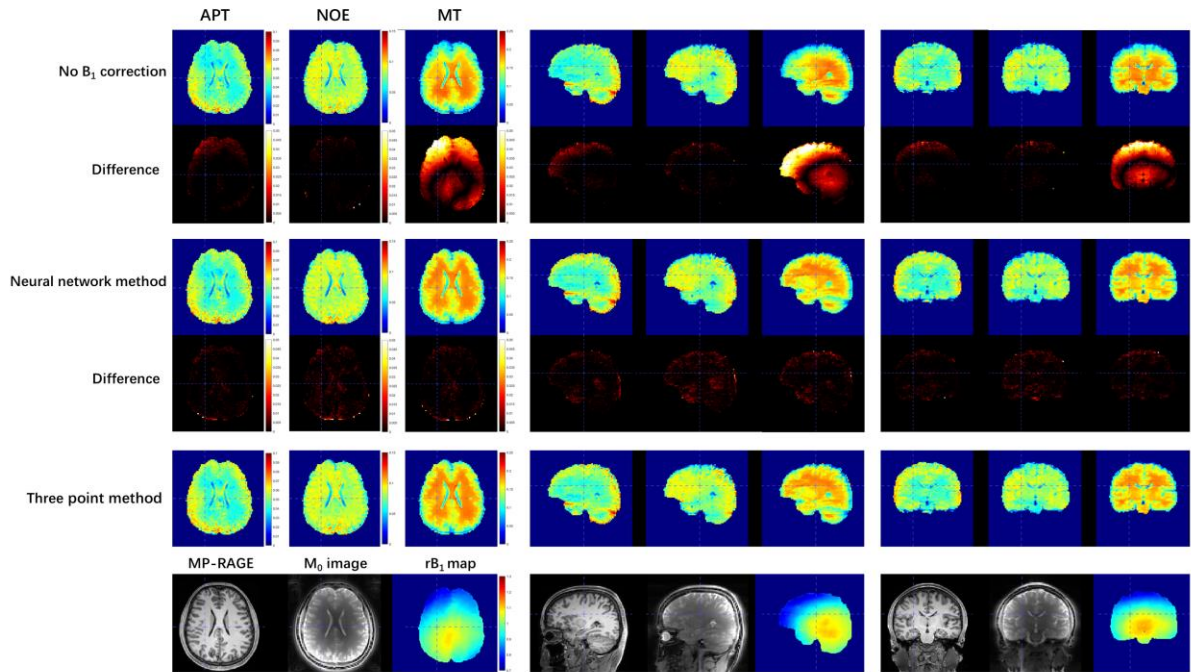


Figure 3. Comparative evaluation of the neural network (NN) for rapid  $B_1$  correction in a healthy subject. Whole-brain MTR<sub>LD</sub> maps for APT, NOE, and MT effects are displayed for three conditions: without  $B_1$  correction, with the proposed NN-based correction, and with the gold-standard three-point method correction. Difference images (NN minus three-point method) show minimal residual signal, indicating a high degree of agreement between the rapid NN method and the gold standard. Reference images, including the  $rB_1$  map, are shown in the bottom panel.

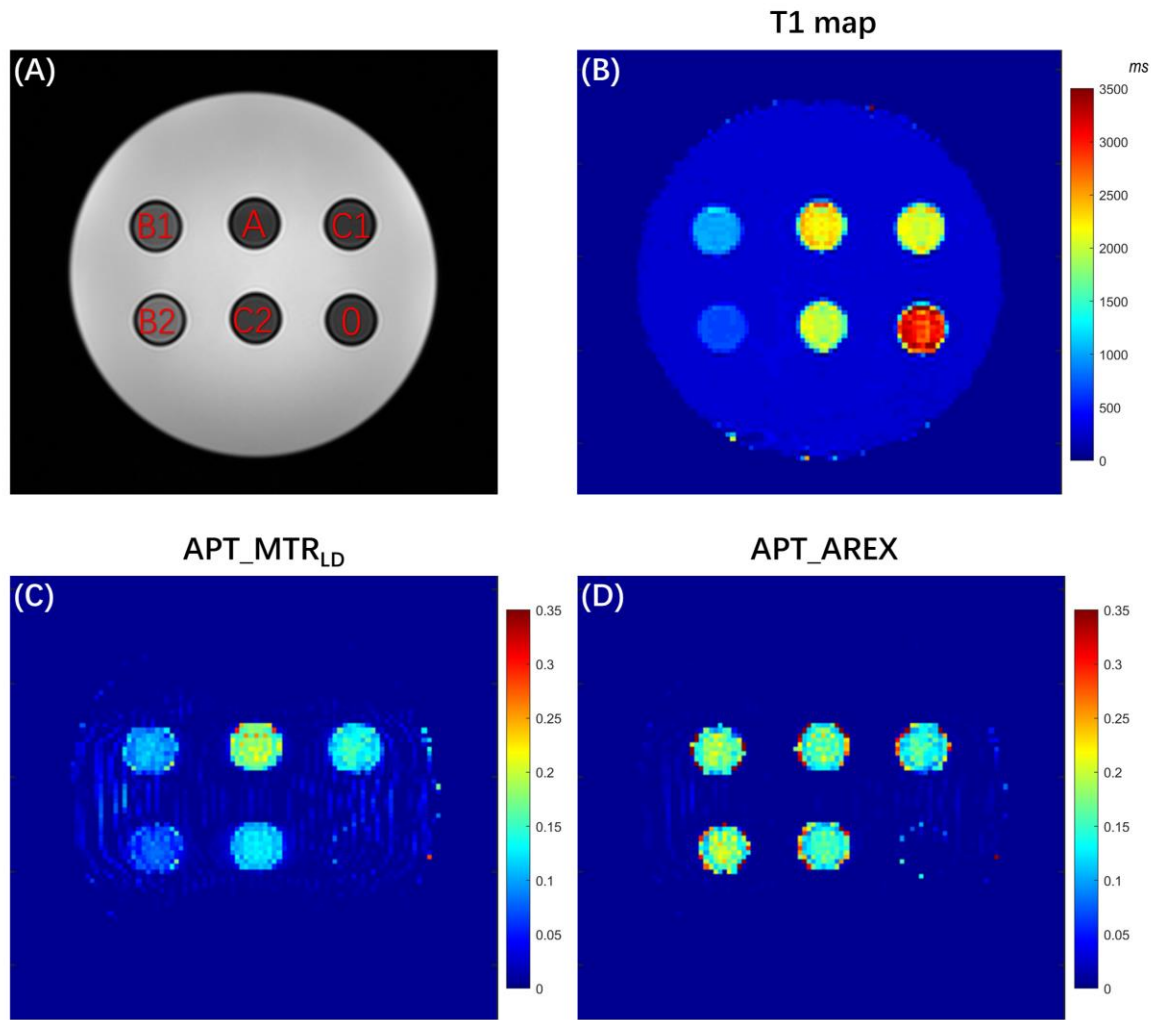


Figure 4. Efficacy of the AREX metric in correcting for confounding T<sub>1</sub> and MT effects. (A) A custom phantom was designed with six test tubes, all at a pH of 7.3. The compositions were: Tube 0, PBS buffer; Tube A, 8% polylysine solution; Tubes B1 and B2, 8% polylysine with 1x and 2x concentrations of a gadolinium contrast agent, respectively, to alter T<sub>1</sub> relaxation; and Tubes C1 and C2, 8% polylysine with 1% and 2% agarose, respectively, to alter magnetization transfer (MT) properties. (B) The corresponding T<sub>1</sub> map confirms T<sub>1</sub> variation across the tubes. (C) The conventional APT\_MTR<sub>LD</sub> map shows significant signal variability across the polylysine tubes, confounded by these T<sub>1</sub> and MT effects. (D) In contrast, the APT\_AREX map demonstrates consistent signal intensity across all five polylysine tubes, successfully isolating the chemical exchange effect from the confounders.

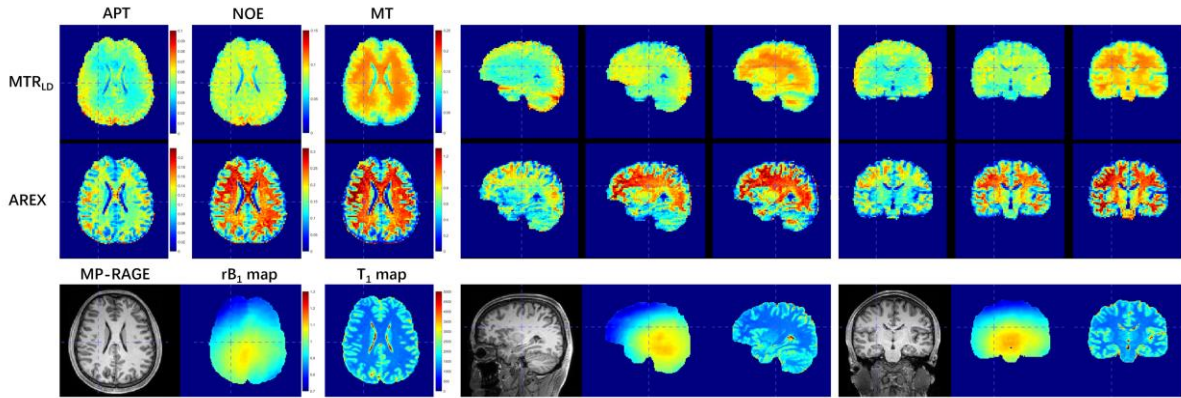


Figure 5. Comparison of whole-brain multi-parameter CEST maps derived from  $MTR_{LD}$  and AREX metrics. Representative axial slices from a healthy volunteer show quantitative maps for APT, NOE, and MT effects calculated using  $MTR_{LD}$  and AREX. Corresponding MP-RAGE,  $T_1$ , and  $rB_1$  maps are provided for anatomical reference. Notably, the AREX maps demonstrate enhanced gray-white matter contrast compared to their  $MTR_{LD}$  counterparts, particularly for NOE and MT effects.

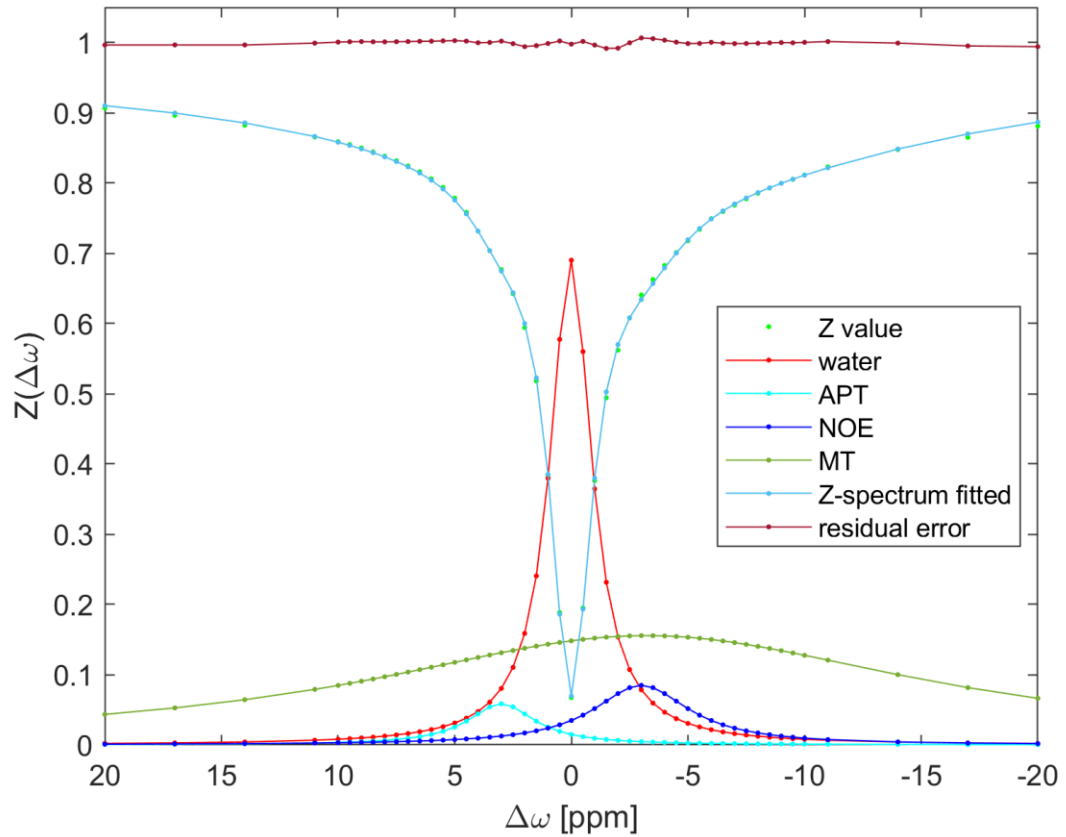


Figure 6. Representative four-pool Lorentzian model fit to in vivo Z-spectrum data. Data from

a voxel in the occipital lobe shows the experimental data points, the overall model fit, and the individual Lorentzian components for water saturation, MT, NOE, and APT. The small fitting residual (top) demonstrates the high quality of the model fit to the acquired data.

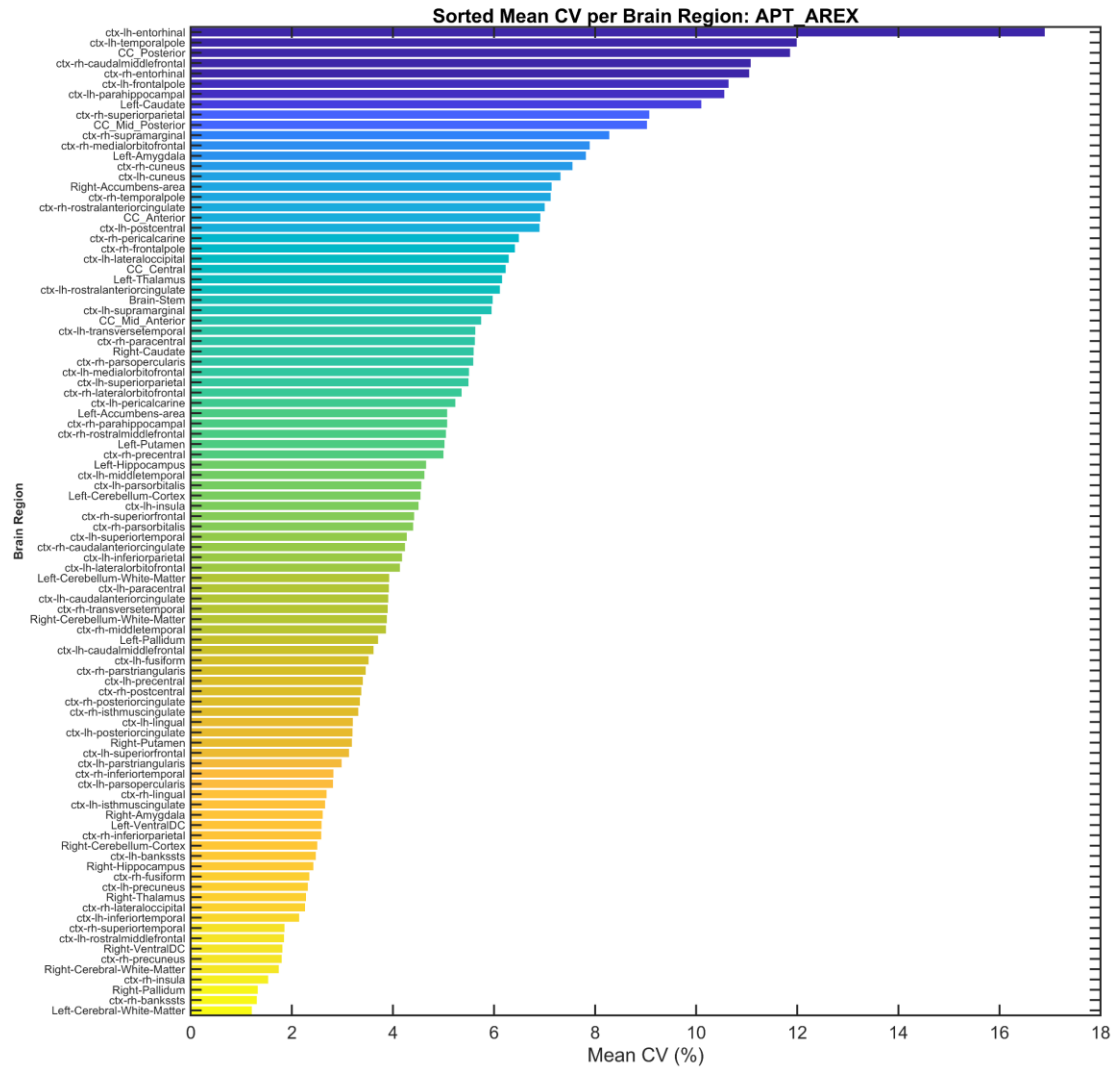


Figure 7. High test-retest reproducibility of the APT\_AREX metric at the brain-region level. The map displays the average coefficient of variation (CV) for APT\_AREX across 96 segmented brain regions. Data were calculated from four healthy subjects scanned on two separate days. The majority of regions exhibit a CV below 10%, confirming the robustness of the proposed method for reliable, region-of-interest-based analysis.

## SUPPORTING INFORMATION

Table S1. MRI Acquisition Parameters for  $B_1$ ,  $B_1$ , and  $T_1$  Mapping.

parameter	Scan 1	Scan 2	Scan 3	Scan 4
<b>Sequence</b>	Spoiled GRE	Spoiled GRE	Spoiled GRE	Spoiled GRE
<b>Flip angle</b>	135°	260°	4°	16°
<b>TR (ms)</b>	35	35	8.4	8.4
<b>TE (ms)</b>	4.2	4.2	2.0/5.8	2.0/5.8
<b>Number of echoes</b>	1	1	2	2
<b>Bandwidth (Hz/pixel)</b>	240	240	350	350
<b>Field of view (mm<sup>3</sup>)</b>	220×220×180	220×220×180	220×220×180	220×220×180
<b>Voxel size (mm<sup>3</sup>)</b>	2.3×2.3×2.5	2.3×2.3×2.5	1.7×1.7×1.7	1.7×1.7×1.7
<b>Orientation</b>	sagittal	sagittal	sagittal	sagittal
<b>Scan time</b>	45s	45s	43s	43s

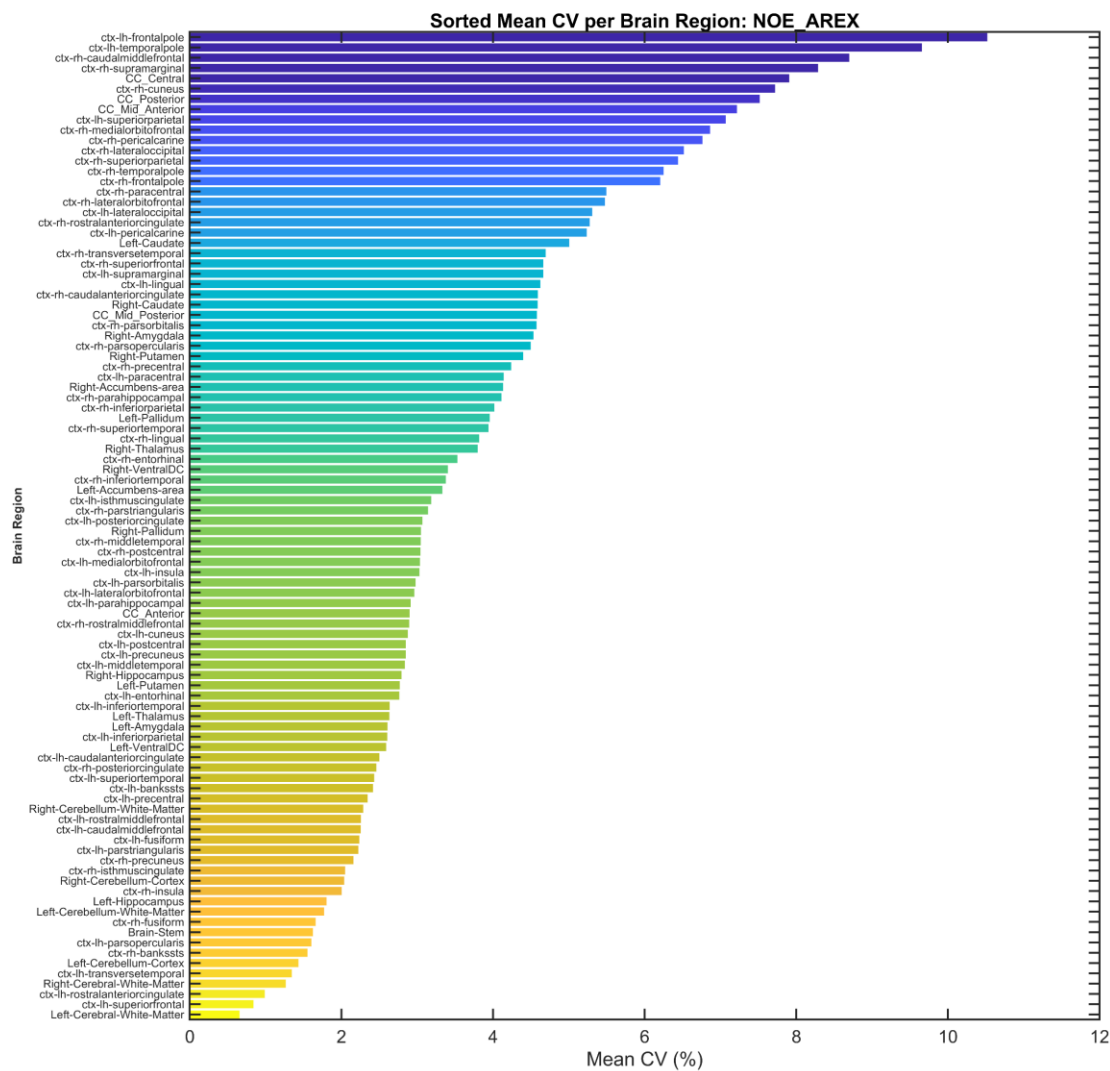


Figure S1. Test-retest reproducibility of the NOE\_AREX metric.

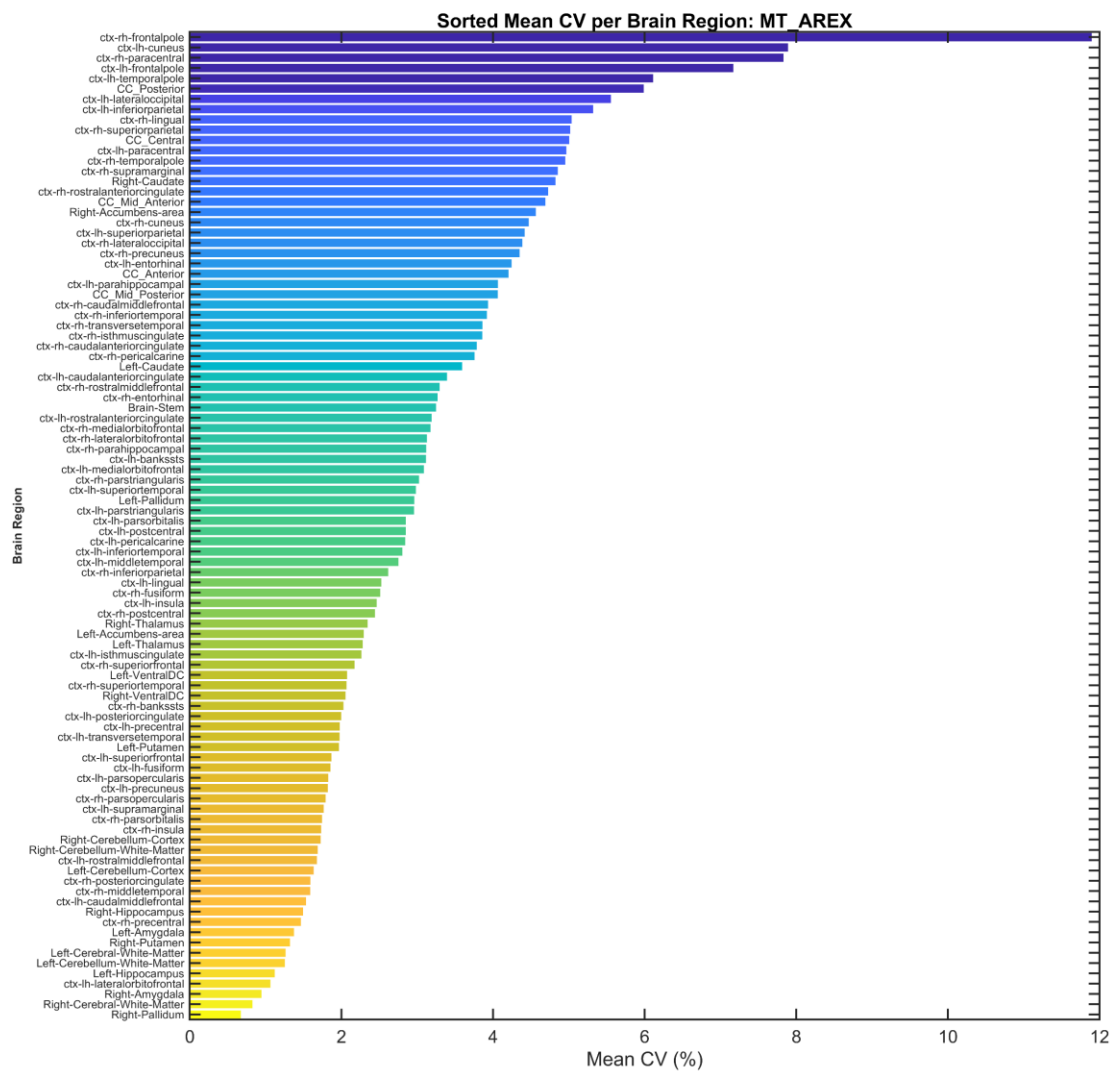


Figure S2. Test-retest reproducibility of the MT\_AREX metric.

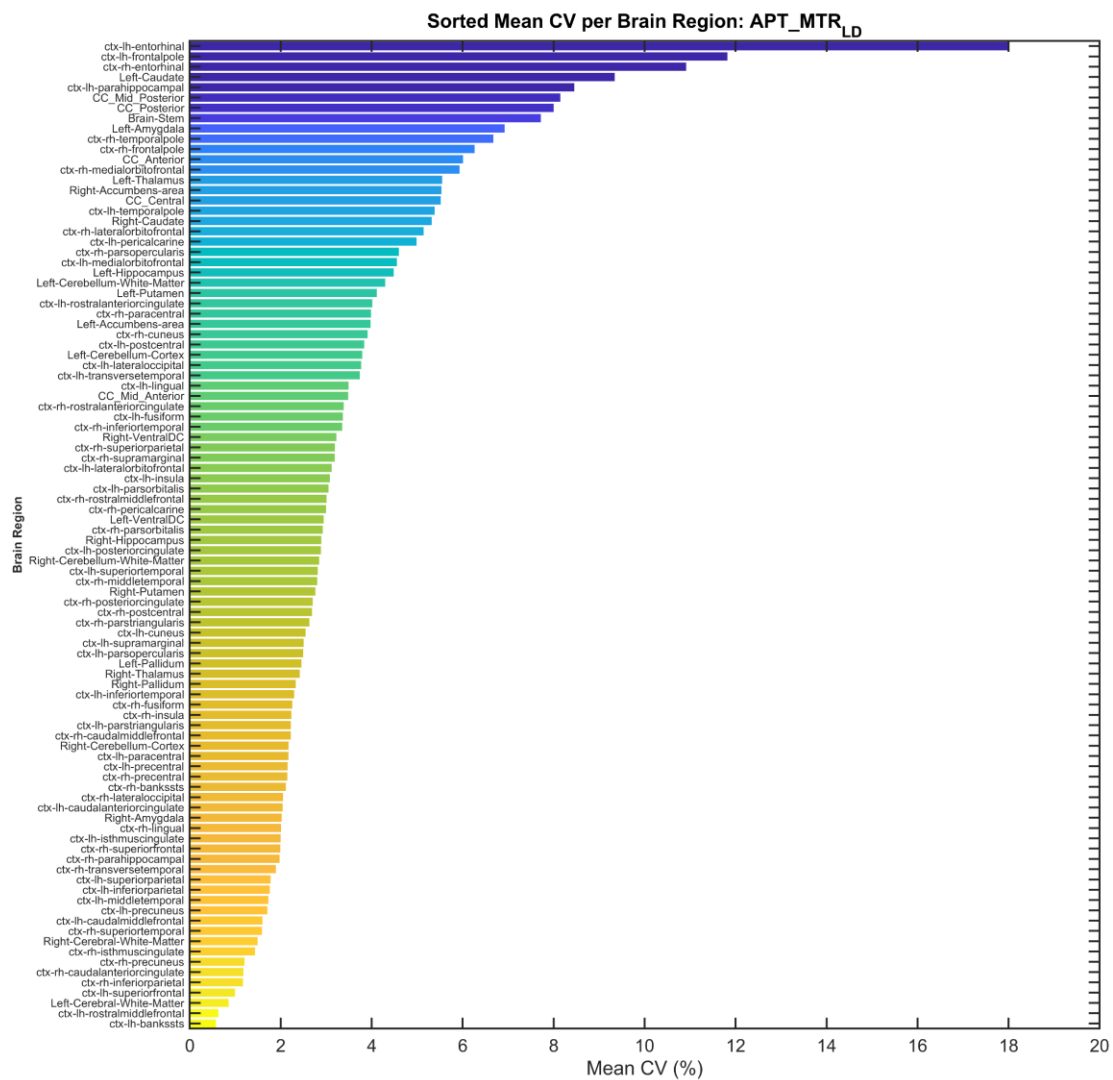


Figure S3. Test-retest reproducibility of the APT\_MTR<sub>LD</sub>.

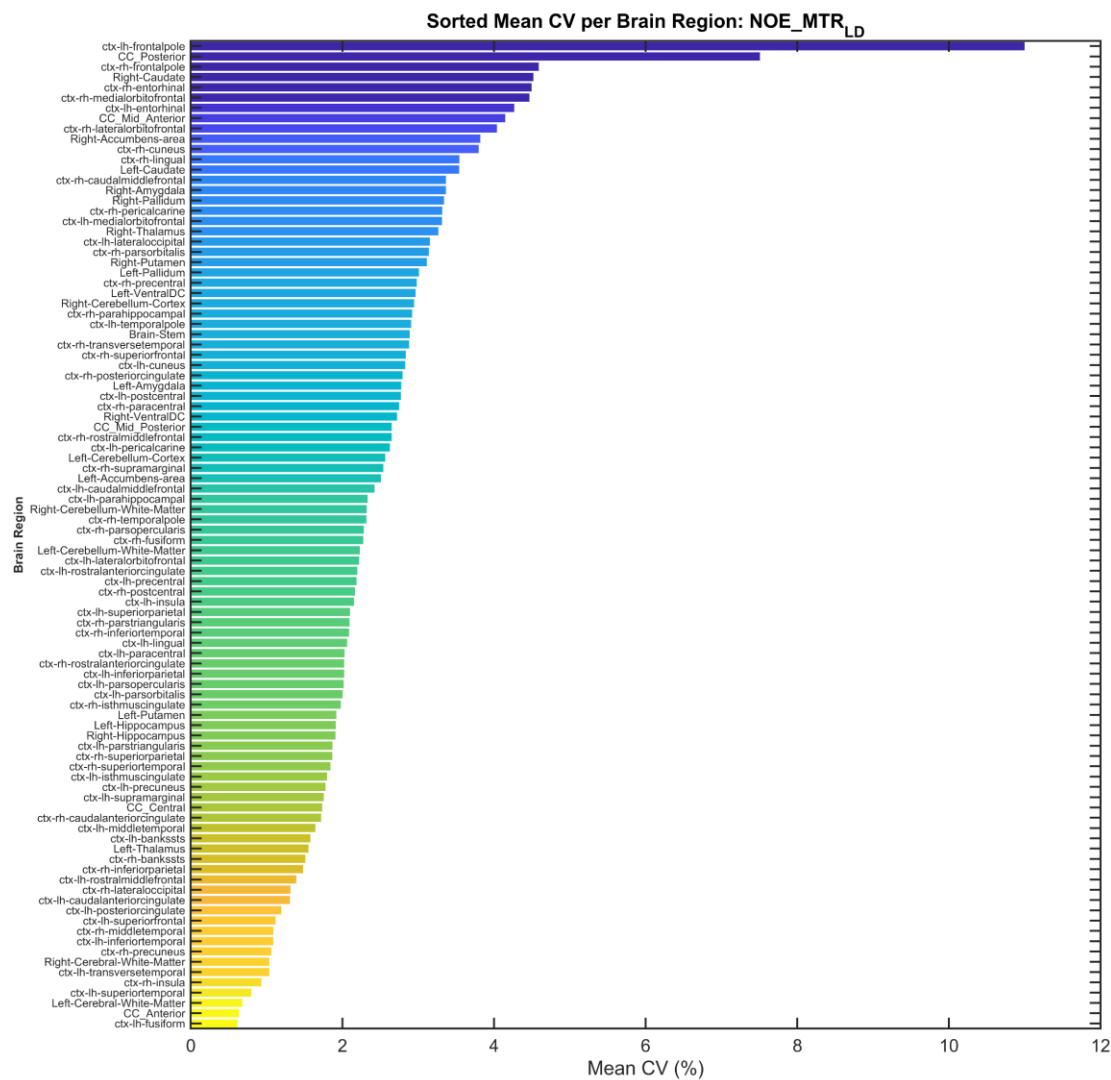


Figure S4. Test-retest reproducibility of the NOE\_ MTR<sub>LD</sub>.

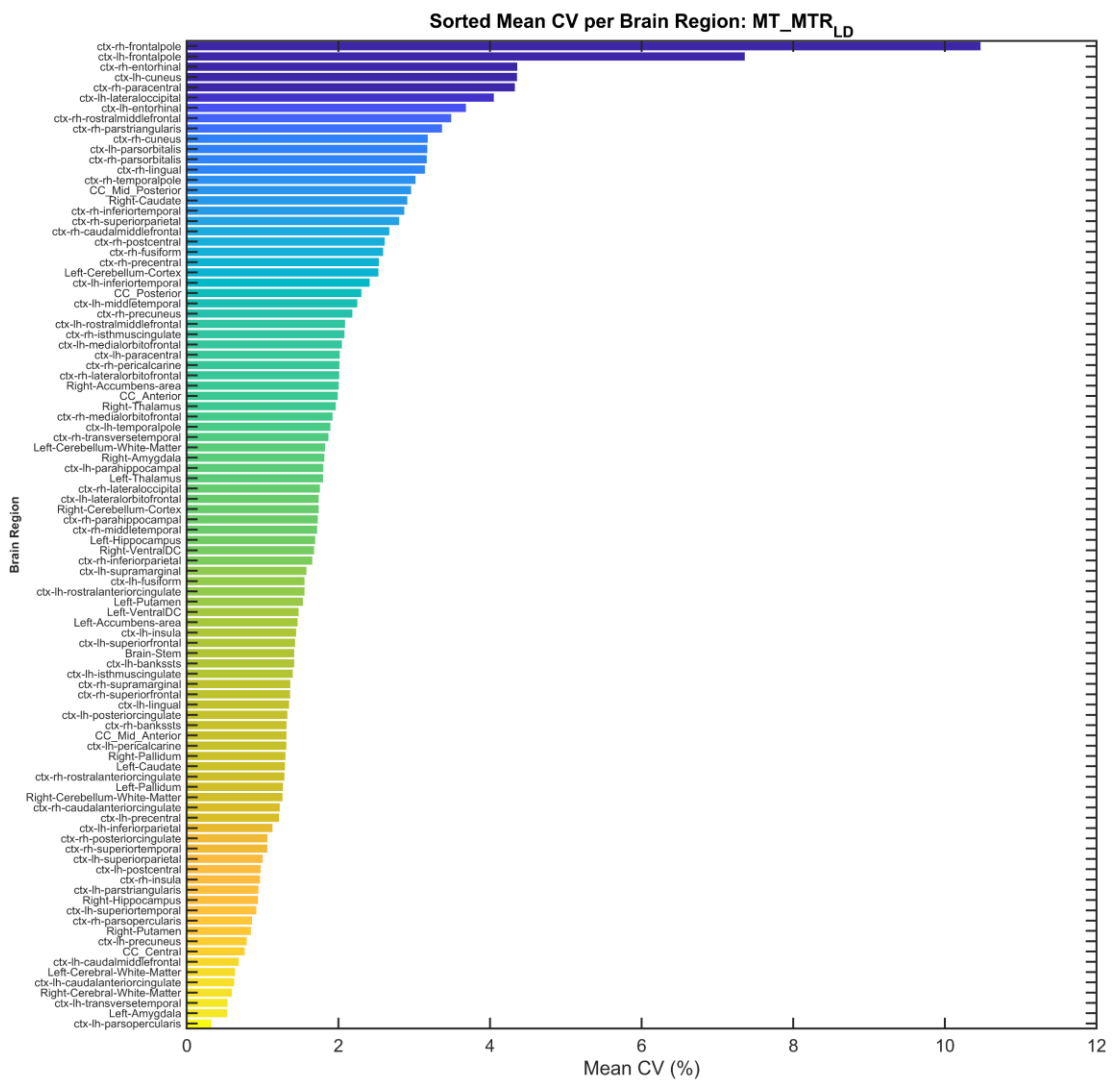


Figure S5. Test-retest reproducibility of the MT\_MTR<sub>LD</sub>.